



# Fluctuating relativistic thin TDE discs

Marc VAN DEN BOSSCHE<sup>1,2</sup> and supervised by Steven BALBUS<sup>2</sup>

<sup>1</sup>*Département de Physique, École Normale Supérieure, 75005, Paris, France*

<sup>2</sup>*Oxford Astrophysics. Denys Wilkinson Building, Keble Road, Oxford, OX1 3RH, United Kingdom*

Internship report  
from April, 6<sup>th</sup> to June, 26<sup>th</sup> 2020

## Abstract

In this report I present original modification to a relativistic thin disc model. This is motivated by unexpected X-rays observation from *UV-only* TDE disc when observed years later by Jonker *et al.* in a recent survey. First I recall the relativistic TDE disc model developed by Balbus and Mummery which has already proven to be able to fit real spectral data. I then propose modifications to this model by varying the disc structure which aim at describing more realistically TDE lightcurve. I present different kind of fluctuations and understand their effect on an accretion disc and its emissions.

# Introduction

The black hole solutions of Einstein equations are known for static, rotating and charged black holes. Yet detecting those highly relativistic compact objects is usually achieved thanks to the radiation emitted by their surroundings. For instance, most observed black holes are encircled by a disc of gas, spiralling towards the hole. The gas of those discs often reaches very high temperatures and emits high-energy light which we can observe from earth.

Accretion discs are of varying size through the universe. Be it a protoplanetary disc around a star or disc around a super massive black hole at the centre of a galaxy, the physics is the same. Matter is in rotation and depending on the strength of the gravitational field it may form new astrophysical objects within itself.

Although it is known that most galaxies have a supermassive black hole in their centre [Magorrian et al., 1998], the majority of neighbouring galaxies does not possess an active nucleus. The lack of a large accretion disc around their supermassive black hole, renders their central black hole more difficult to study and observe. A way to indirectly observe those quiet supermassive black holes is via transient events during the short time period of which we receive a lot of radiated energy. Some of those transient bursts of light correspond to what are called Tidal Disruption Events (hereafter shortened to TDE), during which a star wanders too close to a supermassive black hole and gets torn apart by tidal forces. A portion of the gas of the former star is ejected and is no longer gravitationally bound to the black hole. The other fraction of the gas remains gravitationally bound to the black hole and forms an accretion disc around it. The gas of the disc will undergo considerable heating due to the turbulence therein and reach temperature above  $10^4$  K (e.g. [Holoien et al., 2019]). The gas will hence be very bright, emitting mostly high-energy light like X-rays. Those transient emissions typically last for a time of a few months. Most nearby supermassive black holes are only observable during these events, this is why having a reliable model to describe the evolution of accretion discs created during these is of prime importance for the study of supermassive black holes.

Thus the interesting quantity to model is the light emitted by the accreting gas. The luminosity is a good indicator as it bears information on the temperature and density of the disc gas. The temporal evolution of the luminosity is known for classical Keplerian discs, yet when it comes to super massive black holes, relativistic effects are no longer negligible and requires more work. Although the outer part of the disc is undoubtedly Keplerian, there will be mode coupling with the inner part of the disc. This will have an influence on the evolution of the whole disc [Balbus, 2017]. The observational data is often more precise than just the total luminosity of a transient even. In fact we almost never have access to the full bolometric luminosity of a transient. It is possible to have observe specific spectral bands and their evolution thanks to many recent ground telescopes and space observatories (ASAS-SN<sup>1</sup>, *Swift*,...). This allows for a better knowledge of the temperature and density of the disc gas, and their evolution.

If some of the temporal behaviour of spectral luminosities still remains unexplained by simple current models, it is a way to refine theories and better understand the physics at play in those astrophysical systems.

---

<sup>1</sup>All-Sky Automated Survey for SuperNovæ.

# 1 TDE and disc theory background

## 1.1 Canonical TDE model

The first model for the evolution of debris of a disrupted star was developed at the end of the 1980s [Rees, 1988, Phinney, 1989]. According to this model only a fraction of the stellar mass remains gravitationally bound to the black hole, while the rest of the mass is ejected onto parabolic orbits. Assuming that after disruption, gas particles have a typical energy corresponding to their Keplerian gravitational potential energy, it is possible to know at which rate the bound debris will be swallowed by the hole. Depending on the exact model for the energy distribution, one obtains slightly different mass accretion rates. [Phinney, 1989] obtains a mass accretion rate  $\dot{m}(t) \sim t^{-5/3}$ .

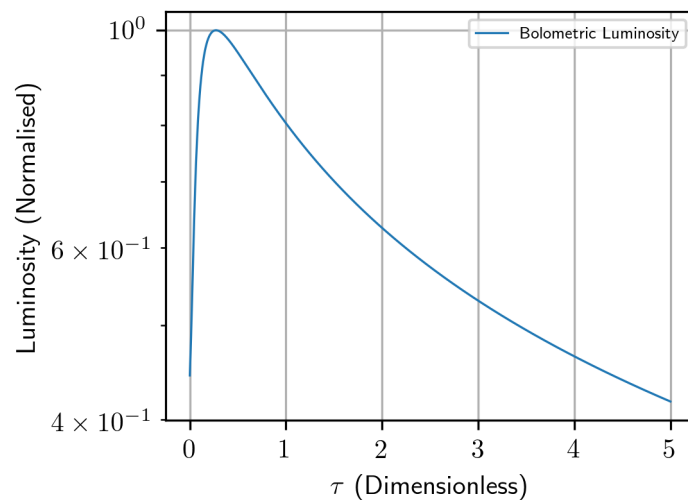


**Figure 1:** This is the typical lightcurve of a TDE model. There is a time lag between when the star get disrupted and when the maximum luminosity is reached. The accretion rate increases during the time when matter piles in the innermost part of the disc. Then the accretion rate decrease in a power law fashion, with  $L(t) \sim t^{-5/3}$ . The typical time scale of such events is a few months. Here  $\tau$  is a dimensionless time, proportional to the usual time  $t$ .

The usual assumption is that the luminosity of the heated gas will follow the behaviour of the accretion rate. Hence,  $L(t) \sim t^{-5/3}$ . A typical TDE light curve is presented on figure 1. On this plot, one can see the two general phases of the disc evolution. The first phase corresponds to matter piling-in at the inner disc boundary. The second phase is the power-law decay of the disc, when mass slowly falls onto the black hole.

## 1.2 Early disc models

The very first disc models date back to the end of the 1940s [von Weizsäcker, 1948]. Yet those models did not match observation unless one invoked an (at the time) unknown angular momentum redistribution mechanism. While some of the disc mass shall fall towards the central gravitational body, the total angular momentum of the disc should be conserved. This implies that the angular momentum is transported outwards by a small fraction of the mass.

The first quantitative evolution model of thin discs was proposed by [Lynden-Bell and Pringle, 1974], who derived a diffusive evolution equation for the surface density of matter in the disc. This model

and the model developed by [von Weizsäcker, 1948] used an *ad hoc* turbulent viscosity between neighbouring fluid layers.

Shakura and Sunyaev [Shakura and Sunyaev, 1973] proposed a model for the turbulent viscosity of such discs. It is parametrised in terms of a dimensionless number  $\alpha$  and the local speed of sound  $c_s$ . This is the standard  $\alpha$ -disc model.

## 2 Recent development in disc models

We now have a better insight on how the angular momentum is transported throughout the disc. [Balbus and Hawley, 1991] proposed a mechanism where this transport is mediated by magnetic fields coupling pairs of particles at different radii and the magneto-rotational instability (MRI). The coupling is similar to one of a masses on spring. The coupling between two particles at different radii induce a torque reducing angular momentum of the particle at smaller radius and increasing the angular momentum of the outermost particle. The slowed particle will then fall at a smaller radius. Likewise, the accelerated particle will move towards the outer regions of the disc.

More recent developments showed that one can obtain the same evolution equation as the canonical model without using an *ad hoc* term. One can obtain the evolution equation by using the weak turbulence formalism [Balbus and Papaloizou, 1999]. This gives rise to a correlation function of radial and azimuthal fluid velocity fluctuation which parametrises the angular momentum transport in the disc in the radial direction. As for many turbulence-related problems, the actual behaviour of this function is poorly known. If we know that magnetic and turbulent stress both play a role, a functional form of this function remains yet to be proposed. For now, this stress can be modelled in a similar to that of the turbulent viscosity of  $\alpha$ -discs.

### 2.1 Relativistic discs

The  $\alpha$ -disc models can be generalised to a fully relativistic geometry [Eardley and Lightman, 1975, Balbus, 2017] as will be presented in part I. Including general relativity to the thin disc formalism is possible and yields a surprisingly simple diffusion equation [Balbus, 2017]. One of the key interest of this relativistic models key interest is that relativistic thin disc with specific boundary condition achieve a shallow luminosity decay fitting observation of the form  $L(t) = t^{-n}$  as shown by [Balbus and Mummery, 2018]. Newtonian models always yield a predicted value of power-law index  $n$  greater than one, which, as we will see, does not match observations.

### 2.2 Limitation of the canonical model

The canonical TDE model mentioned above [Rees, 1988, Phinney, 1989] predicts a power-law decay of the TDE bolometric luminosity at late times  $L(t) = t^{-n}$ , with index  $n = 5/3$ . This model was derived using basic Newtonian dynamics and is still used to distinguish TDE light curves (*e.g.* [Lodato and Rossi, 2010]). Disc models have now been refined and they extend the duration of such events with power-law index  $n \simeq 1.2$  [Cannizzo et al., 1990]. However a recent comprehensive survey of 70 X-rays transient sources, classified as TDEs, report a time behaviour with a shallower  $n \simeq 0.75$  emission decay rate [Auchettl et al., 2017], which can not be explained by the usual TDE models.

### 2.3 Stress condition at ISCO

Solving the evolution equation obtained from the relativistic model with a *finite* stress condition at the *innermost stable circular orbit* (ISCO) of the Kerr geometry yields a value of  $n$  which is

consistently less than unity [Balbus and Mummery, 2018]. This *finite* stress condition is actually subject to discussion. First models claimed that the stress at ISCO had to be *vanishing* [Pringle, 1991, Balbus, 2017] as the solution to the equation with *finite* stress condition at ISCO exhibits violent instabilities at small scales [Balbus, 2017]. This is the case for the viscous stress, which vanishes at the ISCO. Yet more recent studies have shown that a *finite* condition better reproduced the observed data [Balbus and Mummery, 2018, Mummery and Balbus, 2019a], those instabilities remain consistent with a turbulent disc flow. This is because there is a non-vanishing *magnetic* stress at the ISCO (*e.g.* [Noble et al., 2010]). TDEs appear to be a very useful events for determining which of the two stress scenarii is physical as the expected behaviour of luminosity is dramatically different for *vanishing* and *finite* stress conditions.

### 3 Unexplained late time X-ray observations of *UV-only* discs

A recent observation survey [Jonker et al., 2020] reported X-ray detection of several previously detected TDEs, which did not feature X-rays when first observed. All of them had strict upper-boundary at early times for any X-ray emission all of which have been exceeded by a significant amount at later times. The sources are PTF09djl detected nine year prior to the 2019 survey, PTF09axc and PTF09ge detected eight years before Jonker *et al.* observations [Law et al., 2009] and ASASSN-14ae detected in 2014 [Holoien et al., 2014].

All these sources were then classified into the *UV-only* TDE discs category, and agreed with the usual TDE models available at the time. For instance, ASASSN-14ae had been ruled out as an AGN<sup>2</sup> or as a supernova. Moreover this transient source featured constant temperature and a steadily declining luminosity curve, which is characteristic for a TDE [Holoien et al., 2014]. This classification is being questioned by the recent survey and an explanation is yet to be given. In this work, I explore the possibility of new initial conditions on the disc that could have prevented X emission at short times after the TDE, but would allow for X-ray emission in the long run. I present such conditions in part II.

In the first part of this report, I summarise the relativistic thin disc model developed by Balbus and Mummery. I introduce the weak-turbulence formalism that, coupled to the Kerr solution of general relativity black hole gives rise to the diffusion-like disc evolution equation. I also present both analytical and numerical solutions of this equation. Finally I expose how, from those solutions, one can reproduce spectral luminosities which can then be compared to actual observational data. In the second part, I focus on an original modification of the disc model presented in the first part. First I focus on conditions that prevent X-rays emission at early times. Then I expose ways of introducing fluctuation in the disc model at hand and understand their effects.

## Part I

# Relativistic thin discs theory

## 1 A relativistic disc model

The model I use in this work is mathematically quite simple. It is the relativistic generalisation of the usual  $\alpha$ -disc models. This is the model developed in [Balbus, 2017, Balbus and Mummery, 2018]

---

<sup>2</sup>Active Galactic Nucleus

and following papers.

## 1.1 The black hole geometry

For more generality we use the Kerr black hole metric. This black hole geometry corresponds to a spinning black hole. This space-time is determined by only two parameters, the mass of the black hole  $M$  and its angular momentum  $J$ . For simplicity we assume the disc to be in the equatorial plane of the black hole space-time. We hence have the following metric, with  $z$  the rotation axis of the black hole.

$$ds^2 = - \left( 1 - \frac{2r_g}{r} \right) dt^2 - \frac{4r_g a}{r} dt d\phi + \frac{dr^2}{1 - \frac{2r_g}{r} + \frac{a^2}{r^2}} + \left( r^2 + a^2 + \frac{2r_g a^2}{r} \right) d\phi^2 + dz^2 \quad (1)$$

These are the cylindrical Boyer-Lindquist coordinates for the Kerr geometry in the  $z = 0$  equatorial plane.  $a = \frac{J}{Mc}$  is the spin parameter of the black hole and  $r_g = \frac{GM}{c^2}$  the gravitational radius (half of the Schwarzschild radius  $r_s$ ). If we wish to study the Schwarzschild geometry particular case, for a non-rotating black hole, we simply have to set  $a = 0$ .

An implicit assumption we made throughout this work is that we neglect the influence of the disc mass on space-time. Only the black hole of constant mass and spin will bend space-time. This assumption is reasonable as supermassive black holes typically have masses above  $10^6 M_\odot$  and disc masses are only a fraction of a solar masses.

## 1.2 Disc fluid

In the case of a TDE, the gas of the accretion disc comes from one star which was torn apart by tidal forces of the black hole. To study its evolution after disruption, we make use of the canonical general relativity fluid formalism and take advantage of the symmetries of the problem.

### 1.2.1 Relativistic fluid

In order to have a fully relativistic description of the fluid, we use the usual tensor and vector formalism of general relativity. We will use the simple flux conservation equation

$$\nabla \cdot (n\mathbf{U}) = 0, \quad (2)$$

where  $\nabla$  is the covariant derivative,  $n$  is the rest-frame number density and  $\mathbf{U}$  is the fluid 4-velocity. This equation translates the fact that the number of particle in the fluid is constant.

We assume the system to be axisymmetric around the  $z$  axis and we assume that the disc is *thin*, *i.e.* that it does not depend on the  $z$  coordinate. We thus integrate over  $z$  to have a column density  $\Sigma$ .

$$\Sigma = m \int ndz$$

$m$  is the mass of one particle.  $\Sigma$  is thus a surface density. For the stress-energy tensor, we use the usual ideal fluid form to which we add a radiation pressure  $\boldsymbol{\tau}$ .

$$\mathbf{T} = P\mathbf{g} + (P + \rho)\mathbf{U} \otimes \mathbf{U} + \boldsymbol{\tau} \quad (3)$$

$P$  is the pressure of the fluid,  $\rho$  its density,  $\boldsymbol{\tau}$  is symmetric by definition as it is the symmetric tensor product of the radiative energy flow and fluid velocity. We need to include this radiation pressure term as the angular momentum carried by radiated photons is not negligible when the

rotational velocities are of order of the speed of light [Novikov and Thorne, 1973]. As mentioned in this introduction, angular momentum redistribution is a key mechanism in disc dynamics.

Using antisymmetry properties of the Christoffel symbols we obtain the equation

$$\frac{1}{\sqrt{g}}\partial_\mu(\sqrt{g}\sigma_\phi^\mu) = 0 \quad (4)$$

where  $\sigma = \mathbf{T} - P\mathbf{g}$ , and  $g = \det \mathbf{g}$ . We here have an equation on  $\sigma$  because the pressure contribution is negligible, thus we approximate  $\mathbf{T} \simeq \sigma$ .

Note that contrary to steady-state models, we did not assume that the disc does not have temporal evolution. Unlike discs of [Shakura, 1972, Pringle and Rees, 1972, Shakura and Sunyaev, 1973] the accretion disc of a TDE is bound to have a temporal evolution. TDE are by essence transient events. Before the event, there is no disc, and if one waits long enough, the remaining disc after a few years is almost completely depleted.

### 1.2.2 Weak turbulence formalism

We can describe the turbulence in the disc by small velocity departures from some time average velocity. We take the fluctuations to be of vanishing time average.

$$U^\mu = \overline{U^\mu} + \delta U^\mu, \quad \overline{\delta U^\mu} = 0 \quad (5)$$

We assume that the time average velocities correspond to circular orbits of the fluid around the black hole. Those velocities can be computed from the metric. The fluctuations are small departures from this state. This can be written as

$$\delta U_\phi \ll \overline{U_\phi}, \quad \overline{U^r} \ll \delta U^r \sim \frac{\delta U_\phi}{r} \ll r\overline{U^\phi} \quad (6)$$

This will lead us to neglect  $\overline{U^r}$  in the following. We now introduce the stress tensor  $W$  as the average of product of fluctuations, it is a kind of correlation function of the velocity fluctuations. Here we will only be interested in the  $r, \phi$  component, which is defined as

$$\overline{U^r U_\phi} = \overline{U^r} \overline{U_\phi} + W_\phi^r. \quad (7)$$

The correlation function of the angular velocity and the radial velocity  $W_\phi^r = \overline{\delta U^r \delta U_\phi}$  corresponds transport of angular momentum.  $W_\phi^r$  quantifies how the fluctuation of angular momentum  $\delta U_\phi$  is transported by fluid radial velocity fluctuations  $\delta U^r$ . I discuss the boundary conditions of  $W_\phi^r$  in next section.

### 1.2.3 Energetics of the fluid

We assume an equilibrium model in which the energy that the fluid extracts from differential rotation will instantaneously be radiated away at the disc surface. For this equilibrium model, [Page and Thorne, 1974] present the following relationship

$$-\Sigma W_\phi^r \overline{U^0} \frac{d\Omega}{dr} = 2\mathcal{F}, \quad (8)$$

where  $\Omega = \frac{d\phi}{dt} = \frac{\overline{U^\phi}}{\overline{U^0}}$  is the average angular velocity of orbiting particles.  $\frac{d\Omega}{dr}$  is the differential rotation, which also appears in Newtonian disc theory.  $\mathcal{F}$  is the locally radiated energy in the local rest frame. The factor two comes from the fact that both upper and lower sides of the disc radiate.

Using this and equation (4), one obtains the general equation for a thin disc in Kerr geometry

$$\frac{\partial \Sigma}{\partial t} = \frac{1}{\sqrt{g} \bar{U}^0} \frac{\partial}{\partial r} \left[ \frac{1}{\bar{U}'_\phi} \left( \frac{\partial}{\partial r} (\sqrt{g} \Sigma W_\phi^r) + 2\sqrt{g} \mathcal{F} \bar{U}_\phi \right) \right] \quad (9)$$

Dropping the overlines on average quantities and using the variable  $\zeta = \frac{\sqrt{g} \Sigma W_\phi^r}{U^0}$ , one obtains the equation

$$\frac{\partial \zeta}{\partial t} = \frac{W_\phi^r}{(U^0)^2} \frac{\partial}{\partial r} \left[ \frac{U^0}{U'_\phi} \frac{\partial \zeta}{\partial r} \right] \quad (10)$$

This equation has useful analytical solutions in some simplified regimes of interest, this will be more detailed in section 2. I also solved this diffusion-like equation numerically in regimes where no analytical solution is available. Details on numerical integration are exposed in appendix A.1 and A.2.

It is quite convenient that the full relativistic disc evolution is described by a simple diffusion-like equation as equation (10). General relativity operates via the metric and the circular orbits velocities  $U$  that the metric allows.

### 1.3 Boundary conditions

As for any partial differential equation problem, one needs to specify the boundary conditions of the quantities we are solving for. Here there are two types of boundary conditions that require further attention. The first is the behaviour of the stress-energy tensor at the ISCO. The second is the actual density boundary condition at both edges of the integration domain.

#### 1.3.1 Stress condition at ISCO

$W_\phi^r$  is unknown in this problem. Ideally we could compute it from the equations on velocity, but without doing so in GR-MHD 3D simulations, it is hard to get a prescription on it. A way to circumvent this is to use an ansatz for  $W_\phi^r$ . What is often done is to take it to depend on  $r$  the radius in a power-law fashion. We can also model a dependency on the density but in order to do so, equation (10) has to be slightly modified.

$$\frac{\partial \zeta}{\partial t} = \left( W_\phi^r + \Sigma \frac{\partial W_\phi^r}{\partial \Sigma} \right) \frac{1}{(U^0)^2} \frac{\partial}{\partial r} \left[ \frac{U^0}{U'_\phi} \frac{\partial \zeta}{\partial r} \right]$$

The general form for  $W_\phi^r$  I used throughout this work is a double power-law dependency on radius and density.

$$W_\phi^r(r, \Sigma) = w \left( \frac{r}{r_m} \right)^\mu \left( \frac{\Sigma}{\Sigma_0} \right)^\eta \quad (11)$$

Where  $w$  is a constant,  $r_m$  is a typical radial scale and  $\Sigma_0$  is a typical density scale. This is similar to the usual prescription of  $\alpha$ -discs models. However, this functional form for the stress  $W_\phi^r$  is a model idealisation and does not claim to be a realistic description of the real stress. With a such  $W_\phi^r$ , the evolution equation reads

$$\frac{\partial \zeta}{\partial t} = (1 + \eta) \frac{W_\phi^r}{(U^0)^2} \frac{\partial}{\partial r} \left[ \frac{U^0}{U'_\phi} \frac{\partial \zeta}{\partial r} \right] \quad (12)$$

Like the Schwarzschild black hole geometry, the Kerr geometry has what is called an *Innermost Stable Circular Orbit* radius (shortened to ISCO). Below this radius, the assumption we made that the velocity of the fluid  $\mathbf{U}$  was small departures from circular orbits no longer holds, as no circular orbit is possible.

The question of how  $W_\phi^r$  should behave at the ISCO is still uncertain. First theories that it should vanish there [Pringle, 1991, Paczyński, 2000, Balbus, 2017] argued that the short-scale oscillatory behaviour of the Laplace modes of the solutions translated into instabilities. The typical dispersion relation of a Laplace mode  $e^{-st}$  for  $s > 0$  of the inner disc region reads

$$s = \frac{W_\phi^r}{U^0 U_\phi''} \Big|_{r=r_I} k^3, \quad (13)$$

where  $k$  is the wave number of a solution of the form  $\text{Ai}'(kx)$ , with  $\text{Ai}$  the Airy function. This is somewhat similar to the solutions exposed in section 2. Those models claimed those solutions to be unphysical and so justified the need for a vanishing  $W_\phi^r$  at ISCO.

Yet a *finite* ISCO stress appears to yield a better fitting luminosity versus time profile [Balbus and Mummery, 2018] than a *vanishing* ISCO stress does. Models with a *vanishing* stress condition at ISCO consistently produce a  $L(t) \sim t^{-n}$  bolometric luminosity decay at large time with  $n > 1$ . Recent observations [Auchettl et al., 2017] tend to suggest that for real TDE, we have  $n < 1$ . Such a solution is obtained with a *finite* stress condition at ISCO. If it is natural for a viscous stress to vanish at the point where the circular orbits breakdown, it is not the case for the magnetic stress. The fact that magnetic stresses have a important effect in ther innermost regions of disc has been known since a long time [Page and Thorne, 1974, Krolik, 1999, Gammie, 1999]. In the past two decades, numerical studies have shown that the magnetic fields driving MRI, which drives angular momentum transfer in the disc, leads non-zero magnetic stresses at ISCO for extended phases of the disc evolution (*e.g.* [Noble et al., 2010]).

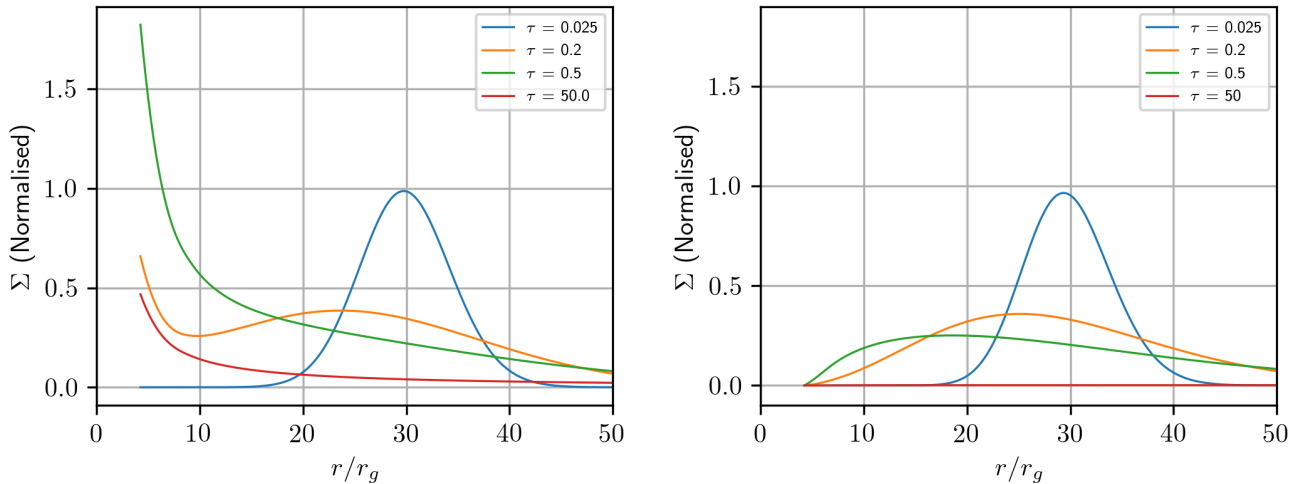
Note that equation (11) implies a *finite* stress at ISCO. When using a *vanishing* ISCO stress condition, I use a piecewise continuous expression of  $W_\phi^r$ . Above  $10r_g$ , I use expression (11), and below I take  $W_\phi^r \propto (r - r_I)^2$ .  $r_I$  is the ISCO radius.

### 1.3.2 Density boundary condition

**At ISCO** The sensible ISCO condition for density depends on whether we impose *finite* or *vanishing* stress tensor there. For a vanishing ISCO stress, one should impose  $\zeta(t, r_I) = 0$  *i.e.* density does not diverge there (as  $\zeta \propto \Sigma W_\phi^r$ ). For a finite ISCO stress, one should impose  $\partial_r \zeta(t, r_I) = 0$ . The latter condition correspond to the fact that the density will equilibrate instantaneously thanks to the non-vanishing density current  $y = \sqrt{g} \Sigma W_\phi^r$  at ISCO.

**At infinity** The physical condition that should be imposed is  $\Sigma(t, r = \infty) = 0$  as we assume that no mass can reach infinity in a finite time. However for numerical integration, it is not possible to integrate on a infinite box. I imposed a vanish gradient condition  $\partial_r \zeta(t, r_{\max}) = 0$ . It allows mass to flow rimwards without being stuck at the outer boundary, as a strict condition there would do.

When imposing a vanishing gradient, be it at ISCO or at infinity, some mass is lost from the integration box. One should be aware of it but it is not a problem, as it is expected that mass will fall onto the black hole and that some, carrying angular momentum will flow outwards.


 (a) Disc with *finite* ISCO stress.

 (b) Disc with *vanishing* ISCO stress.

**Figure 2:** This plot represents the surface density of the disc at different times. The initial condition is a Dirac delta at  $30r_g$ . It smooths out and then falls towards the black hole. Note that the inner most point of the curves corresponds to ISCO radius, below which the integration can not be carried out. The run of figure 2a used a *finite* stress condition at ISCO. The run of figure 2b used a *vanishing* stress condition at ISCO. The  $\tau$  time scale is defined in equation (14).

Figure 2a presents the evolution of the density with a *finite* ISCO stress condition. One can see the initial Dirac delta condition first smooths out and spreads both towards the black hole and rimwards. Then the mass proceeds to fall towards the black hole and piles-in near the ISCO. Slowly the disc matter is accreted onto the hole and the disc mass decreases. The general behaviour of the evolution of a disc with *vanishing* stress at ISCO is similar. However, as can be seen on figure 2b, the depletion of such a disc is much more rapid. At  $\tau = 50$ , the disc with *vanishing* stress condition is completely depleted.

On this figure, the time scale used is a dimensionless one defined in [Balbus and Mummery, 2018] as

$$\tau = \frac{t}{t_v} = \frac{16q^2}{\gamma^2 r_0^{2q}} t \quad (14)$$

where  $t_v$  is the viscous time scale.  $q = \frac{3-2\mu}{4}$  where  $\mu$  is the power law dependency of  $W_\phi^r$  on the radius.  $\gamma^2 = 2r_m^\mu \sqrt{\frac{GM}{w^2}}$ , where  $M$  is the black hole mass,  $G$  is Newton gravitation constant,  $w$  is the multiplicative factor of  $W_\phi^r$ .  $r_0$  is the initial condition disc radius and  $r_m$  is the same as in the definition of  $W_\phi^r$  in equation (11).

## 1.4 Initial condition

The initial conditions for this diffusion problem are somewhat less important than the boundary conditions. Indeed the long term evolution of the disc does not depend on the exact form of the initial condition [Balbus and Mummery, 2018].

The initial condition for the matter distribution that I use throughout this work consists of a initial Dirac delta function at some initial radius  $r_0$ ,  $\delta(r-r_0)$ . This corresponds to an infinitesimally radially thin ring at this radius. For the numerical integration I carry out, this naturally translates into a numerical Dirac delta *i.e.* a Kronecker delta function  $\delta_{r,r_0}$ . The normalisation of the initial condition corresponds to the initial mass of the disc. This is a fraction of the mass of the disrupted star.

## 1.5 Bolometric luminosity

From the density profiles we obtain by solving equation (10), one can compute the total luminosity emitted by the accretion disc. Using the energy flux  $\mathcal{F}$  defined in equation (8), the luminosity reads

$$L(t) \propto \int_0^\infty \sqrt{g_{rr}g_{\phi\phi}} \frac{\mathcal{F}}{(U^0)^2} dr \quad (15)$$

However we do not integrate the equation for radii below the ISCO, we thus ignore this part of the disc in terms of luminosity. We also neglect any relativistic ray tracing effects here. Numerical integral computation was carried out using a Simpson algorithm, see appendix A.3 for more details.

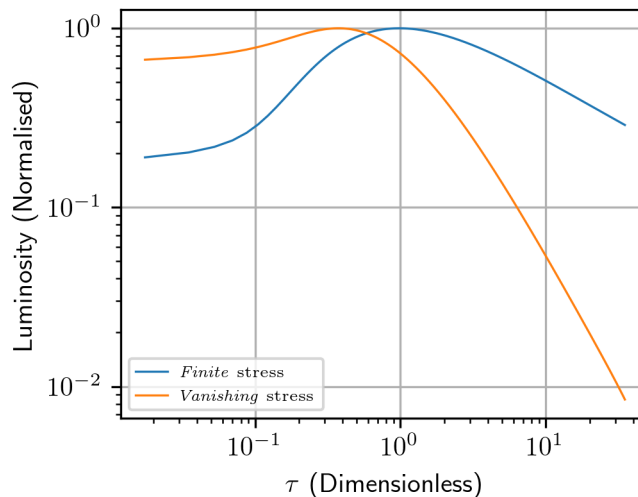


**Figure 3:** This is a comparative plot of bolometric luminosity light curve for both stress conditions at ISCO. The luminosities are normalised by their maxima. Both decay in a power law fashion at large time,  $L(t) \sim t^{-n}$ . The orange curve is the luminosity of a disc with a *vanishing*  $W_\phi^r$  ISCO stress, its decay is such that  $n > 1$ . The blue curve represents the luminosity decay of a disc with *finite* stress at ISCO. It decays more slowly, with  $n < 1$ .

It is this luminosity function that reportedly has a shallower decay than what the canonical disc models predict. However as discussed in the previous section, using a *finite stress condition* at ISCO allows for a better agreement with observational data. Figure 3 presents a plot of the bolometric luminosity with both ISCO stress conditions. The difference between the two light curves is noticeable. The luminosity of a disc with *vanishing* stress condition at ISCO decreases by two orders of magnitudes in the same time during which the luminosity of the *finite* stress disc only reaches half of its initial value. The only difference between the two curves of this figure is the stress boundary condition at ISCO. This difference of accretion rate can also be seen on figure 2, where the disc with *vanishing* stress at ISCO is depleted much more rapidly.

## 2 Solutions of the model

Here we aim at solving equation (10) for radii larger than the ISCO radius, hence determining most of the disc mass evolution. I only present the *finite* stress at ISCO solution, at it has already been shown to be a better fit for observations [Balbus and Mummery, 2018, Mummery and Balbus, 2019a]. First we shall assume that at large radii, and down to some radius  $r_m$ , the angular momentum gradient of the disc fluid  $\frac{dU_\phi}{dr}$  is the Keplerian angular momentum gradient. We assume that below

radius  $r_m$ , the angular momentum gradient is linear in  $r$  and matches the Keplerian one at  $r_m$ . It is reasonable to make this prescription for the inner region as, in full general relativity,  $\frac{dU_\phi}{dr}$  vanishes at the ISCO.

$$\frac{d\tilde{U}_\phi}{dr} = \begin{cases} \sqrt{\frac{2r_g}{r_I^3}}(r - r_I) & \text{for } r_I < r < r_m, \\ \frac{1}{2}\sqrt{\frac{GM}{r}} & \text{for } r > r_m. \end{cases} \quad (16)$$

We also assume a constant stress  $W_\phi^r(t, r) = w$ . We do so for simplicity and because once the ISCO condition is set, the results are not very sensitive to the exact parametrisation of the stress [Balbus and Mummery, 2018]. Hence, equation (10) becomes

$$\frac{\partial y}{\partial t} = \frac{w}{\sqrt{2}\Omega_I} \frac{\partial}{\partial x} \left[ \frac{1}{x} \frac{\partial y}{\partial x} \right] \quad \text{for } r_I < r < r_m, \quad (17)$$

$$\frac{\partial y}{\partial t} = \frac{2w}{\sqrt{GM}} \frac{\partial}{\partial r} \left[ \sqrt{r} \frac{\partial y}{\partial r} \right] \quad \text{for } r > r_m. \quad (18)$$

Where  $y = \zeta U^0 = \sqrt{g}\Sigma W_\phi^r$ ,  $x = r - r_I$ ,  $\Omega_I = \sqrt{\frac{r_g}{r_I^3}}$  and the joining condition is continuity of  $y$  and  $\frac{\partial y}{\partial r}$  at  $r_m$ . One can examine the corresponding Laplace mode equations with time dependence  $e^{-st}$  for  $s > 0$

$$-\frac{s\sqrt{2}\Omega_I}{w}y = \frac{d}{dx} \left[ \frac{1}{x} \frac{dy}{dx} \right] \quad \text{for } r_I < r < r_m, \quad (19)$$

$$-\frac{s\sqrt{GM}}{2w}\xi y = \frac{d^2y}{d\xi^2} \quad \text{for } r > r_m, \quad (20)$$

where we use  $\xi = \sqrt{r}$ . These equations have well known solutions, they read

$$y = \text{Ai}'(-kx), \quad k^3 = \frac{s\sqrt{2}\Omega_I}{w}, \quad \text{for } r_I < r < r_m, \quad (21)$$

$$y_\pm = \sqrt{\xi} J_{\pm\frac{1}{3}} \left( \frac{2q}{3} \xi^{\frac{3}{2}} \right), \quad q^2 = \frac{s\sqrt{GM}}{2w}, \quad \text{for } r > r_m. \quad (22)$$

$\text{Ai}$  is the Airy function and  $J_p$  is the standard Bessel function of order  $p$ . Above the matching radius, we have a superposition of both solution (both  $+\frac{1}{3}$  and  $-\frac{1}{3}$  order Bessel functions). The superposition integral at large radii reads

$$\int_0^\infty J_p(\sqrt{s}X) J_p(\sqrt{s}X_0) e^{-st} dt = \frac{1}{t} \exp\left(\frac{-X^2 - X_0^2}{4t}\right) I_p\left(\frac{XX_0}{2t}\right) \quad (23)$$

where  $X_0$  is the initial disc radius and  $I_p$  is the modified Bessel function of order  $p$ . The numerical solution, for example figure 2, is in agreement with this analytical result. As shown in [Balbus and Mummery, 2018], for a *vanishing* ISCO stress condition, the solution with Bessel function of order  $p = +\frac{1}{3}$  dominates. For a *finite* ISCO stress, it is the negative order  $p = -\frac{1}{3}$  which dominates.

### 3 Spectral evolution of a relativistic thin disc

We are able to predict the bolometric luminosity of an accretion disc, yet it is not easy to compare those results with actual observations. Even though observations of black hole accretion discs are performed at different wavelengths ranging from optical light to X-rays, observation of a single disc is often achieved at a few wavelengths only. Furthermore the telescope often does not have a wide

spectral range and to obtain a complete spectrum of a single object, one needs several observations. It is thus useful to be able to predict the behaviour of a disc in term of a given wavelength emission. Moreover some frequencies of light are impossible to observe from earth, namely extreme UVs. Without observing them, it is impossible for us to obtain the full bolometric luminosity.

### 3.1 Black body model

The simplest model one can take is to assume that the disc is a multi-temperature black body. For a one dimensional disc model like described in section 1, the temperature will be a function of the radial distance only. The temperature can be computed in the thin disc formalism as

$$\sigma T^4(t, r) = -\frac{U^0(r)U^\phi(r)}{2r} \frac{\Omega'(r)}{\Omega(r)} \zeta(t, r) \quad (24)$$

$\sigma$  is the Stefan-Boltzmann constant. The usual relativistic black body equation reads, for the emitted luminosity between two frequencies

$$F_X(t) = \int_{\nu_\ell}^{\nu_u} \int_S \frac{2h\nu_o^3}{c^2} \frac{1}{e^{\frac{h\nu_o}{k_B T}} - 1} d\Theta_o d\nu_o \quad (25)$$

$h$  and  $k_B$  are Planck's and Boltzmann's constants respectively.  $d\Theta_o = \frac{d\alpha d\beta}{D^2}$  is the solid angle under which the system is observed, where  $\alpha$  and  $\beta$  are photon impact parameters at infinity and  $D$  is the distance between observer and the disc.  $\nu_e$  and  $\nu_o$  are the emitted and observed frequencies respectively.  $\nu_\ell$  and  $\nu_u$  are the lower and upper frequencies of the band we wish to model.  $f = \frac{\nu_o}{\nu_e}$  can be computed using the metric and depends only on  $r$  if we assume that the disc lies on the equatorial plane as in section 1. Indeed

$$f = \frac{1}{U^0} \frac{1}{1 + \frac{p_\phi}{p_0} \Omega}, \quad (26)$$

where  $\mathbf{p}$  is the 4-angular momentum of an emitted photon in the local rest frame which can be obtained by solving  $\mathbf{p} \cdot \mathbf{p} = 0$  for the photon. This takes ray tracing into account, with general relativistic geometry.

It is convenient to define an effective temperature  $\tilde{T}$  such that

$$\tilde{T}(r, t) = f(r)T(r, t) \quad (27)$$

Hence, we rewrite the observed flux

$$F_X(t) = \int_{\nu_\ell}^{\nu_u} \int_S \frac{2h\nu_o^3}{c^2} \frac{1}{e^{\frac{h\nu_o}{k_B \tilde{T}}} - 1} d\Theta_o d\nu_o \quad (28)$$

With this model, it is quite simple to access emission at specific energies from the density profiles, which we obtain from solving equations of section 1. This model has achieved fitting of observed sources [Mummery and Balbus, 2020]. Those fits are presented on figures 4. The presented curves are fits to the source ASASSN-14li [Holoien et al., 2015]. The analytical curve on figure 4a can be obtained taking the quasi-Wien limit ( $h\nu \gg kT$ ) of equation (28) and using the fact that the peak temperature of the disc behaves as

$$T_p \sim \tau^{-n/4}.$$

This behaviour for the peak temperature can be obtained using a self-similar disc solution as described in [Pringle, 1991].

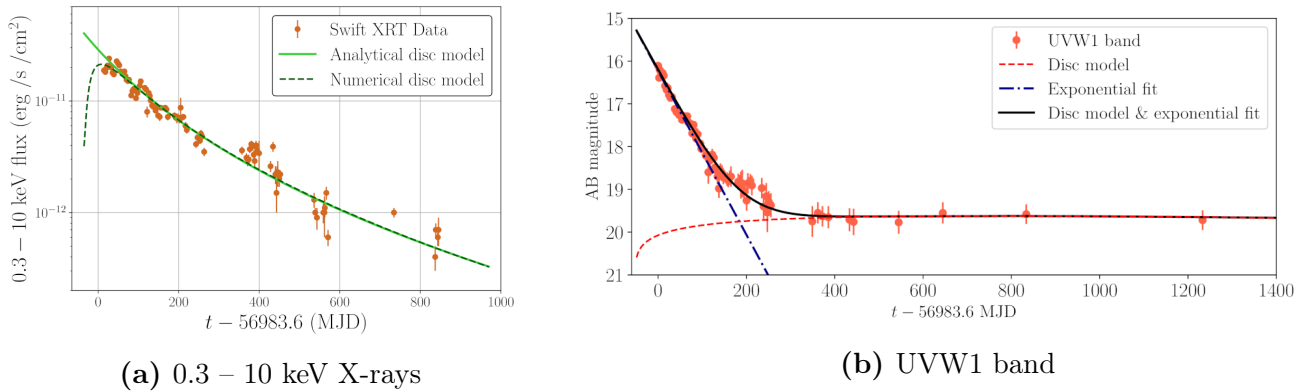


**Figure 4:** These are the plots presented in [Mummery and Balbus, 2020]. They show how the light curves produced with this model compare to actual ASASS-14li observations. Figure 4a compares the numerical integrated disc model (dashed green curve), with the analytical disc model (light green curve) and ASASS-14li data (orange dots). The curves, both analytical and numerical fit the observed data. Figure 4b shows how the UV emission, modelled as presented in this report, also fits the observed data. It compares the disc model of part I (dashed red curve), an exponential fit (black dashed line), the sum of the exponential model and the disc model (black curve) and the observed data (orange dots).

Note that on figure 4b, an exponential term of the form  $F_0 \exp\left(-\frac{t-t_D}{t_{UV}}\right)$  is added to fit the curves ( $t_D$  is the time at which the TDE begins and  $t_{UV}$  is some UV time scale). This is because at early times the physics included in the model presented here is not enough to model the light emission. Discs can be messy at early times and phenomena like clumping of matter may happen and strongly change the emission. The usual way of modelling this missing physics is with an exponential decay term for the UV emission [Holoien et al., 2015]. Note that the actual cause of this exponentially decaying emission is not known, it might even not be coming from the disc itself.

### 3.2 Approximations

For simplicity’s sake, in this work I use a somewhat simplified model. I do not take into account the ray tracing effects. This translates into using a simpler expression of the ratio  $f$

$$f \simeq \frac{1}{U^0}. \quad (29)$$

The effective temperature I use is defined as in equation (27), but its values will be slightly different.

This first part furnishes a complete model for TDEs and the evolution of the disc formed from debris of the disrupted star. This model has been refined in a series of paper [Balbus, 2017, Balbus and Mummery, 2018, Mummery and Balbus, 2019a, Mummery and Balbus, 2019b, Mummery and Balbus, 2020] and we now know more about the specific conditions that one shall use to model a realistic TDE event. For instance, contrary to what was thought at early stages, a *finite* stress condition at ISCO appears to be physical and better fits observations. This model provides us with a way to obtain theoretical spectral light curves both analytically and numerically.

## Part II

# New results

If the observed lightcurves of real TDE are well fitted by the model presented in part I, the observed values always exhibit small departures from the theory. The precision of the instruments used for these detection are nowadays such that those departures should be trusted as real physical phenomena. An example of a fluctuating light curve of a TDE is presented on figure 5. How the model I present in this part for fluctuations can describe it is discussed below.

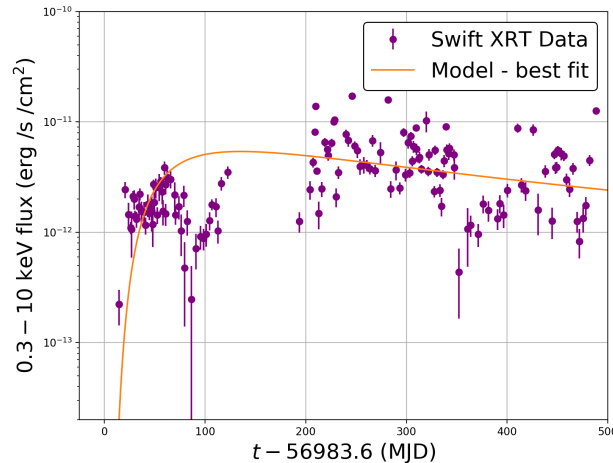


**Figure 5:** This is a plot of the raw and binned observed X-rays luminosity of AT2018fyk [Wevers et al., 2019]. This sources has a temporal gap of X-rays emission between days 100 and 200 after first detection. This gap could correspond to a depletion event. This figure is courtesy of A. Mummery.

Some of the departures suggest that some physics is missing in the model I presented. A good example for some missing physics is that the model of part I does not predict the early UV behaviour of ASASSN-14li (figure 4b), as discussed above. One had to add by hand the exponential term corresponding to early times TDE disc physics, which was not included in the model of part I.

In this part, I present different modifications to the model presented in the first part in which I truncate the disc and vary its density distribution. I examine how those modification affect the disc and the produced lightcurves.

## 1 Truncated discs

The spectral time evolution of actual TDE disc is not very well known. This is because the available theoretical TDE models are simplified models and they fail to explain the exact 3D dynamics of the disc gas. The approximations made in those models often are reasonable enough to well describe actual TDEs. For instance [Mummery and Balbus, 2020] fitted ASASS-14li observation data. However some discs appear to feature more complicated dynamics that the current models yet fail to describe. For example several discs that have been classified into *classical* UV-only scenario four to nine years ago have recently been observed anew and featured X-ray emission [Jonker et al., 2020].

This can be caused by a lot of different phenomena, including emission mechanism that is not included

in the relativistic thin disc model presented in part I. However one can try and include by hand some of the consequences of this physics in the model and observe and quantify the modifications that it induces on the disc evolution.

Such a treatment can be proposed for the initial state of the disc. We can imagine that the inner edge of the disc is not at ISCO, but at some greater radius. This could be because of some peculiar dynamics close to the black hole such as ultra relativistic jets blowing matter that gets too close. It is also possible that the innermost part of the disc could be unstable, causing it to be constantly depleted. We can model this by truncating the disc at early times, assuming that all the mass falling below  $r_t$  is either swallowed by the hole, or blown out of the disc, either way, this is mass which is lost for the disc. This peculiar dynamics is also to end at some time  $t_e$  after the beginning of the TDE. This translates into new boundary conditions for equation (10).

Similarly to the condition we used in part I, we impose, at all times, a vanishing gradient for  $\zeta$  at the outer boundary

$$\frac{\partial \zeta}{\partial r}(r_\infty, t) = 0. \quad (30)$$

For times before the truncation condition is lifted, at times  $t < t_e$ , we also impose the density below the truncation radius to be vanishing

$$\zeta(r, t) = 0, \quad \text{for } r < r_t \quad (31)$$

Finally, after the truncation is lifted, at times  $t \geq t_e$ , we impose the usual vanishing gradient condition on  $\zeta$  at the ISCO radius

$$\frac{\partial \zeta}{\partial r}(r_I, t) = 0. \quad (32)$$

Note that before  $t_e$ , the inner disc condition is the same as if we imposed a *vanishing* stress there. As discussed in [Balbus and Mummery, 2018] and in part I of this report, this means that the disc will decay more rapidly in this first phase, be it the disc mass or its luminosity.

## 1.1 Analytical solution

The equation of the problem stays the same : it is equation (10). Like in section 2, we assume that at large radii, the angular momentum gradient is Newtonian.

We divide the resolution in two steps: The first phase is when the disc is truncated, then the second phase is when it is not.

Like above, we assume a constant  $W_\phi^r = w$  and we also assume  $r_t < r_m$  such that the truncation radius is in the relativistic region.

### 1.1.1 Phase 1: Truncated disc evolution

Because of the  $\zeta = 0$  inner boundary condition, this part is the same as before as with *vanishing* stress condition. The equations read

$$\frac{\partial y}{\partial t} = \frac{w}{\sqrt{2}\Omega_I} \frac{\partial}{\partial x} \left[ \frac{1}{x} \frac{\partial y}{\partial x} \right] \quad \text{for } r_t < r < r_m, \quad (33)$$

$$\frac{\partial y}{\partial t} = \frac{2w}{\sqrt{GM}} \frac{\partial}{\partial r} \left[ \sqrt{r} \frac{\partial y}{\partial r} \right] \quad \text{for } r > r_m, \quad (34)$$

and the Laplace mode truncated solutions are

$$\tilde{y}_{\text{tr},1}(s, r) = \text{Ai}'(-kx), \quad k^3 = \frac{s\sqrt{2}\Omega_I}{w}, \quad \text{for } r_t < r < r_m, \quad (35)$$

$$\tilde{y}_{\text{tr},2}(s, r) = \sqrt{\xi} J_{-\frac{1}{3}} \left( \frac{2q}{3} \xi^{\frac{3}{2}} \right), \quad q^2 = \frac{s\sqrt{GM}}{2w}, \quad \xi = \sqrt{r}, \quad \text{for } r > r_m. \quad (36)$$

It is implicit that for  $r < r_t$  we have  $\zeta(r) = y(r) = \Sigma(r) = 0$  in this first phase. Note that the *vanishing* condition at  $r_t$  has the same effect on the solution as the *vanishing* stress tensor solution, but at  $r_t$  rather than  $r_I$ .

In each region, to have the real time-solution, one has to do inverse Laplace transform.

$$y_{\text{tr},i}(t, r) = \frac{1}{2\pi i} \int_{\gamma-iT}^{\gamma+iT} e^{st} \tilde{y}_{\text{tr},i}(s, r) ds \quad (37)$$

As we are working with Bessel functions, it is quite convenient that  $I_\alpha(x) = i^{-\alpha} J_\alpha(ix)$ .

We call  $Y_{\text{tr}}(t, r)$  the continuous function defined at all times  $0 < t < t_e$

$$Y_{\text{tr}}(t, r) = \begin{cases} 0, & \text{if } r < r_t, \\ y_{\text{tr},1}(t, r), & \text{if } r_t \leq r < r_m, \\ y_{\text{tr},2}(t, r), & \text{if } r \geq r_m. \end{cases} \quad (38)$$

### 1.1.2 Phase 2: Back to usual *finite* stress solution

In the second phase, the equations still are equations (33) and (34), yet the initial conditions are different. We do not have a Dirac delta but the state of the truncated disc at time  $t_e$ . The solutions will have the same form, yet the integration constants will be different.

$$\tilde{y}_{f,1}(s, r) = \alpha_1 \text{Ai}'(-kx) + \beta_1 \text{Bi}'(-kx), \quad k^3 = \frac{s\sqrt{2}\Omega_I}{w}, \quad \text{for } r_I < r < r_m, \quad (39)$$

$$\tilde{y}_{f,2}(s, r) = \alpha_2 \sqrt{\xi} J_{-\frac{1}{3}} \left( \frac{2q}{3} \xi^{\frac{3}{2}} \right) + \beta_2 \sqrt{\xi} J_{\frac{1}{3}} \left( \frac{2q}{3} \xi^{\frac{3}{2}} \right), \quad q^2 = \frac{s\sqrt{GM}}{2w}, \quad \xi = \sqrt{r}, \quad \text{for } r > r_m. \quad (40)$$

where  $\alpha_i$  and  $\beta_i$  are such that the joining condition is time-continuity at all radii

$$\forall r > r_I, Y_f(0, r) = Y_{\text{tr}}(t_e, r),$$

where  $Y_f(r, t)$  is the continuous function defined at all times  $t > 0$

$$Y_f(t, r) = \begin{cases} y_{f,1}(t, r), & \text{if } r_I \leq r < r_m, \\ y_{f,2}(t, r), & \text{if } r \geq r_m. \end{cases} \quad (41)$$

## 1.2 Numerical solution

Solving the equations in the truncated case numerically is no problem. One has to implement conditions (30),(31) and (32) in the numerical solver developed in part I.

### 1.2.1 General solution

The first confirmation that we have is that, the two phases indeed look like the *vanishing* stress case for the first phase, and like the *finite* stress case for the second phase. The decay, be it of mass or luminosity, has a higher rate in the first phase. We can compare the luminosity plotted on figure 7c with the light curves of figure 3. In the first phase, one has a rapidly decaying power law with  $n > 1$  while in the second phase we have a shallower  $n < 1$ . In the second phase, we witness a so called *stalled* accretion [Mummery and Balbus, 2019a].

Figure 6, shows the density evolution of such a truncated disc. Both phases are clearly distinguishable. First the disc evolves accordingly to usual *vanishing* stress models [Balbus, 2017, Pringle, 1991]. Debris of the star pile in near the inner boundary and slowly accrete through this boundary. When the truncation is lifted, the remaining gas falls towards the ISCO. This is somewhat similar to the usual evolution of a disc with *finite* stress condition at ISCO.

Param.	Value
$a/r_g$	0.5
$M$	$1.85 \times 10^6 M_\odot$
$m$	$1.63 \times 10^{-2} M_\odot$
$\mu$	0
$\eta$	0
$t_e/t_v$	5
$r_t/r_g$	15
$r_0/r_g$	30

**Table 1:** These are the parameters used for the run with a truncated disc.  $m$  is the mass of the disc. In order to have sensible parameter values, I use the same parameter values as the parameters that achieved a fit of ASASSN-14li presented in [Mummery and Balbus, 2020]. The parameters I added are the three last lines of this table, concerning truncation. This is not to reproduce a particular observation, but rather to observe the general behaviour of a truncated disc.

Note that in table 1, the truncation time is taken at a value larger than  $t_v$ . This is because  $t_v$  is the viscous time scale *i.e.* it is the time that the disc takes to go from its initial condition to its “equilibrium” state. This “equilibrium” state corresponds to a density distribution with no memory of the initial condition. An example of such a distribution, is the  $\tau = 50$  curve (red) of figure 2. Taking any  $t_e > t_v$  has a similar effect on the disc. The remaining mass after  $t_e$  will change, but the general behaviour is unchanged. I take such a value of  $t_e$  to let the disc reach this state before removing the truncation.

The effect of the truncation on the disc seems to have varying effect depending on the mean of observation. For instance, there is little effect on the UV emission, as shown on figure 7. This is because the UV light is emitted on a much larger region of the disc as, unlike X-rays, it does not require extreme temperature of the gas. The same figure also shows that at first there is no X-ray emission. This is because the density of the disc, and thus its temperature, are not high enough. The truncation, when released, gives rise to a X-ray peak. This peak is also a feature of the bolometric luminosity. This is due to matter piling up at the inner edge of the disc, and thus reaching very high densities and temperatures. For both the X-rays and the bolometric luminosity, the peak after truncation is at a lower intensity than for disc which is not truncated. This is because, although the density near the ISCO becomes very high, the overall mass of the disc has decreased since its

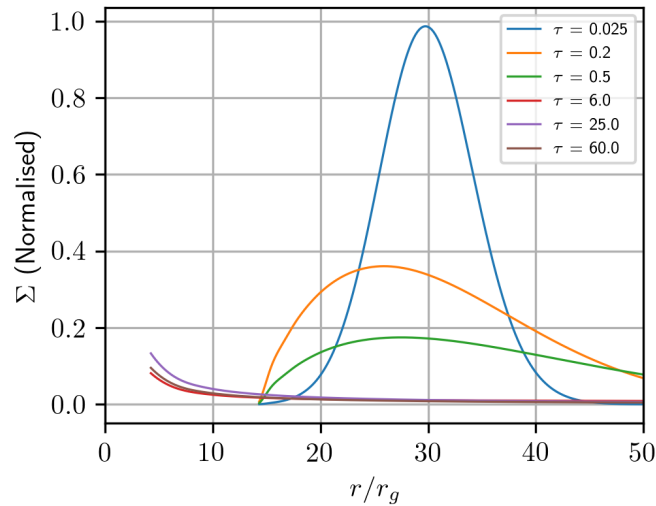


**Figure 6:** Surface density of the disc at different times. The parameters of this run are specified in table 1. One can clearly see the two phases of the dynamics. First matter piles-in near  $r_t$  at times  $\tau = 0.025, 0.2, 0.5$ . The truncation is relaxed at  $\tau = 5$ . The remaining matter then falls toward the ISCO in the usual fashion (see part I) at times  $\tau = 6, 25, 60$ .

initial value. The parameters of this run are the same as those used to produce the numerical curve of figure 4a. One can notice that the peak here is almost a thousand times less bright. This is due to the accretion of mass during the first phase of evolution.

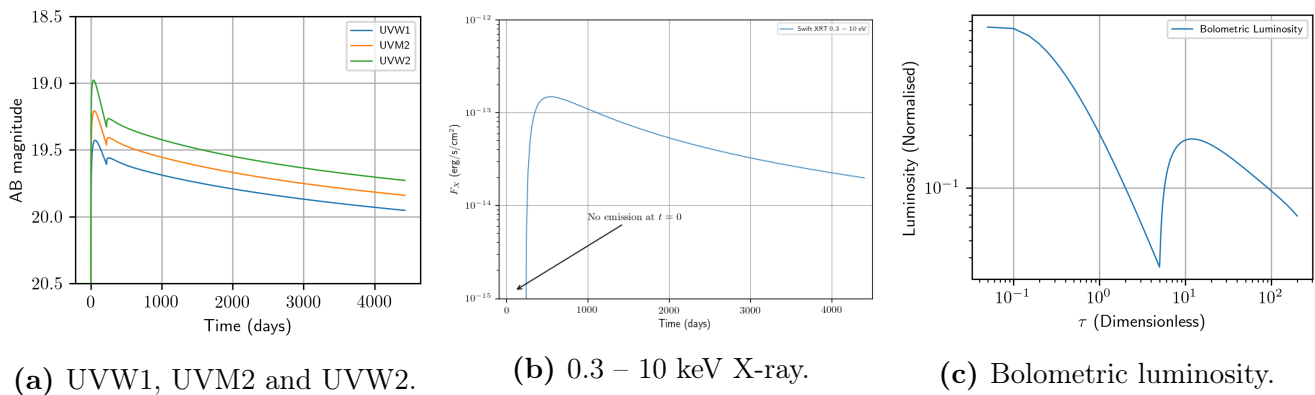


**Figure 7:** The two first figures are mock Swift observations, of both its UV bands and X band. The third figure is the total bolometric luminosity of the disc. The parameters of this truncated disc are presented in table 1. The labels of the curves indicate the truncation radius. The UV lines emission do not change by much after the truncation is released. However the truncation prevents any detectable X-ray emission prior to  $t_e$ .

### 1.2.2 Effect of truncation radius

The parameter of the truncation that one can easily change is the radius at which the truncation happens. It is not obvious how changing it will affect the luminosities of the disc. The truncation radius shall be put to comparison with both the ISCO radius and the initial radius of the disc. Getting close to either of them might have different effects.

Param.	Value
$a/r_g$	0.5
$M$	$1.85 \times 10^6 M_\odot$
$m$	$1.63 \times 10^{-2} M_\odot$
$\mu$	0
$\eta$	0
$t_e/t_v$	5
$r_0/r_g$	15

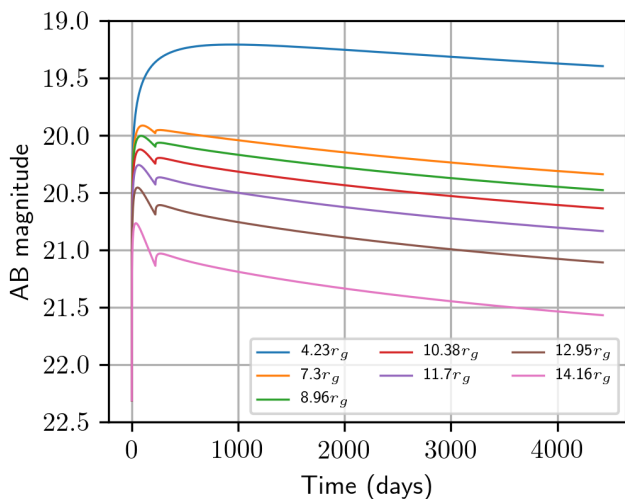
(a) Parameters kept constant

ID	Param.	Value
1	$r_t/r_g$	4.23
2	$r_t/r_g$	7.30
3	$r_t/r_g$	8.96
4	$r_t/r_g$	10.38
5	$r_t/r_g$	11.70
6	$r_t/r_g$	12.95
7	$r_t/r_g$	14.16

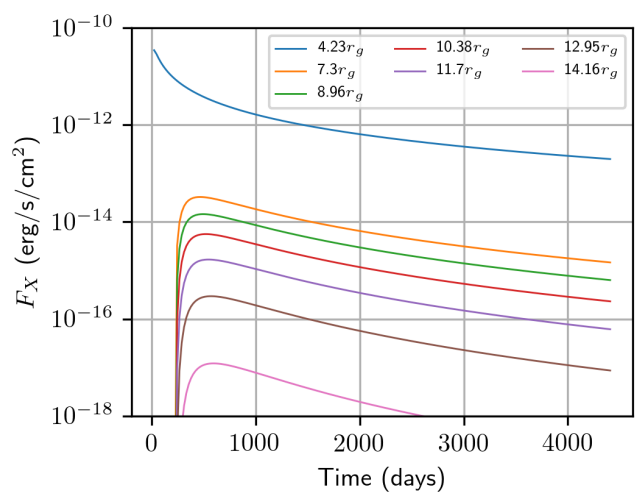
(b) Varying parameter

**Table 2:** These are the parameters used for the comparative runs with truncated discs. Here too the disc mass, black hole mass and spin are taken from the fitting values of ASASS-14li [Mummery and Balbus, 2020]. Note that run #1 has truncation at ISCO, this is equivalent to letting the disc evolve in the first phase with *vanishing* ISCO stress.

In the limit  $r_t = r_I$ , nothing special happens, it is the normal disc evolution with *vanishing* stress condition at ISCO during the first phase. This is illustrated on figure 8, see the curves with parameter  $r_t = 4.23r_g$  (blue curves). Yet for a truncation slightly above the ISCO radius, the effect is strong. Values of  $r_t$  tested are presented in table 2.



(a) UVM2 line



(b) Swift X-rays

**Figure 8:** These plots are the mock Swift UV and X-rays lightcurves for truncated discs. This plot compares the lightcurves of discs which only differ by their truncation radii  $r_t$ . The curves label correspond to the parameters listed in 2. In all cases the UV emission is less affected by the truncation that the X-rays emission is. Unless for run # 1, there is not X-rays emission in the first phase of evolution, when the disc is truncated.

The light curves for different truncation radii are plotted on figure 8. One can see that like in the previous case, the UV emission is rather unaffected by the truncation. The X-rays emission is dramatically modified. For untruncated discs, there is X-rays emission right from the start. Here, it is the case only when  $r_t = r_I$ , the ISCO radius. Otherwise the density is not high enough at the inner disc edge during the first phase.

A larger truncation radius  $r_t$  induces X-ray luminosity peak at later times. The matter that piled-in at the truncation radius, has a longer way to fall before reaching the ISCO and piling up again there.

It is this secondary piling-in that produces very high temperatures within the disc gas, hence the X-ray emission. However the larger the truncation radius, the less bright the disc is in the X-rays. This is due to the fact that during the first phase more mass is accreted onto the black hole because the truncation radius is closer and closer to the radius of the initial Dirac ring.

As I used physically reasonable values for the parameters, the absolute values of the obtained light curves make sense. For the largest truncation radii tested, it is possible that the X-rays light would be below the detection thresholds of telescopes as it is thousands of times dimmer than the actual ASASSN-14li observation.

This could also be a possible scenario for the observed late time only X-rays [Jonker et al., 2020]. The disc of those TDE could have been truncated for a long time by some yet unknown physical mechanism. The truncation could have ended some time between the first detection and the recent survey by Jonker *et al.* This would allow for a late X-rays emission compatible with the absence of X-rays in the first times.

## 2 Periodic depletion

In this section, I explore the effect of a periodic depletion of some of the disc mass. This could be used to model fluctuating sources. I first examine the general effects of a periodic depletion of the innermost part of the disc. I then study the influence of the truncation radius for this kind of fluctuations.

### 2.1 Sharp depletion of the inner disc

The innermost part of the disc can be subject to different instabilities and those may lead to a rapid depletion of its inner matter. Here I model, in a somewhat similar fashion to previous section, the sudden depletion of the inner part of a TDE disc. I let the disc evolve normally and every  $T_d$ , I remove all matter below some depletion radius  $r_d$ . This depletion is instantaneous. Analytically this would happen exactly when  $t \equiv 0 \pmod{[T_d]}$ . Numerically, the depletion lasts only for one time step, the disc is free to flow back in the inner region right after it.

Unlike for truncated discs discussed in section 1, this is not equivalent to the *vanishing* stress case. The stress is always *finite* at ISCO and not particular condition other than  $\zeta(t = kT_d, r \leq r_t) = 0$  for  $k \in \mathbb{N}^*$  is imposed at  $r_t$ .

For simplicity, the depletion is modelled at periodic. This is an idealised model, which do not claim to fit any observed source.

Like in section 1, I choose a value of the depletion period such that  $T_d > t_v$ . This is so that the disc density distribution has time to reach a state with no memory of the previous depletion. Additional effects may arise if we take  $T_d$  shorter than the viscous time scale. For instance, the total disc mass could decrease rapidly if the over-density wave corresponding to the peak density in the first phase were to be completely depleted before having time to spread again.

The run presented in figure 9, the parameters of which are in table 3, is the result of such a periodic depletion. One can notice that, like in the simple truncation case, the UV are not affected a lot by the periodic depletion. Apart from the small fluctuation, these light curves is similar to usual untruncated discs like the one used to fit ASASSN-14li data.

However the X-ray emission, coming for the most part from the innermost part of the disc, is strongly dimmed by each depletion. For instance the first depletion event reduces the luminosity by a factor close to  $10^4$  before it comes up again. If the upper envelope of the X-rays light curves looks similar

Params.	Value
$a/r_g$	0.5
$M$	$1.85 \times 10^6 M_\odot$
$m$	$1.63 \times 10^{-2} M_\odot$
$\mu$	0
$\eta$	0
$r_0/r_g$	30
$T_d/t_v$	5
$r_d/r_g$	15

**Table 3:** These are the parameters of the periodic depletion run. Those values are also taken from [Mummery and Balbus, 2020] for the most part. This allows sensible comparison of the obtained light curves with the ASASSN-14li data. I take  $T_d/t_v > 1$  to let the disc settle down between each depletion event.

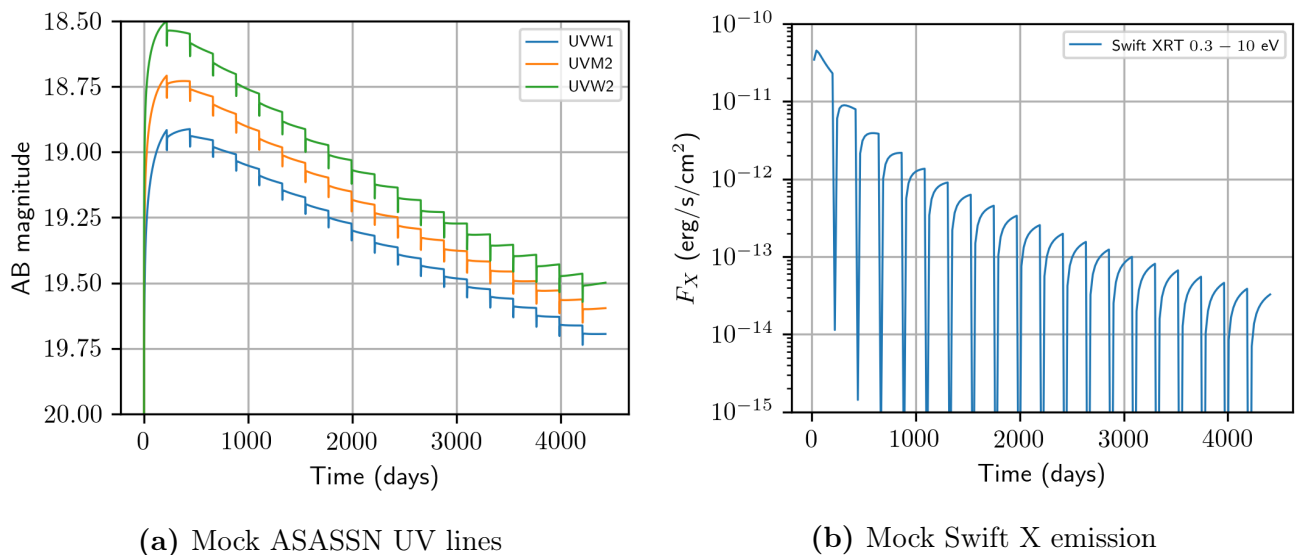


**Figure 9:** These plots are UV and X-rays lightcurves produced by a periodically depleted disc. The parameters for this run are in table 3. The X-rays is strongly affected by the repeated depletion. However the UV lines emission is significantly less affected. The upper envelope of both light curves are similar to usual undepleted disc. The effect of the depletion is a fluctuation of the emitted light.

to the one of ASASSN-14li, its fluctuations are a lot stronger. It is also noteworthy that contrary to the truncated disc scenario, the luminosity is quite high for the X-rays, comparable to the luminosity of ASASSN-14li. This is because the first phase of the truncated disc evolution gave rise to a long and strong mass depletion period. Here mass is lost only instantaneously at each depletion event. Moreover, as I take  $T_d > t_v$  the disc has time to smoothly spread before being depleted again. So doing minimises the mass loss during depletion events.

This plot could correspond to a fluctuating source, where some complicated dynamics periodically remove the innermost part of the disc. Some of the X-ray luminosity point might even be under the detection threshold at their lowest, then come back up just before the next depletion.

## 2.2 Influence of the depletion radius

Like for truncated discs, the depletion radius plays an important role in the lightcurves of periodic depletion events. Here too it is interesting to see how much the depletion radius influences the X-rays and UV emission depending on how it compares to the ISCO radius and the initial Dirac ring radius.

Param.	Value
$a/r_g$	0.5
$M$	$1.85 \times 10^6 M_\odot$
$m$	$1.63 \times 10^{-2} M_\odot$
$\mu$	0
$\eta$	0
$T_d/t_v$	5
$r_0/r_g$	30

(a) Parameters kept constant

ID	Param.	Value
1	$r_d/r_g$	4.23
2	$r_d/r_g$	8.96
3	$r_d/r_g$	14.16
4	$r_d/r_g$	16.48
5	$r_d/r_g$	19.83

(b) Varying parameter

**Table 4:** Parameters used for the comparatives runs with truncated discs. The constant parameters are the same as in table 3. Here too the values of the parameters are the ones for the fit of ASASSN-14li. Note that run #1 has truncation radius at ISCO. See figure 10.

Here, in the limit  $r_t = r_I$ , it is not equivalent to the *vanishing* stress condition at ISCO. The depletion is instantaneous, and apart from when  $t \equiv 0 \pmod{[T_d]}$ , the disc is free to evolve with the *finite* ISCO stress condition. The depletion for  $r_t = r_I$  will have a small effect, it will only remove the mass exactly at ISCO. For numerical integration, this corresponds to setting  $\zeta_0^t$  to 0.

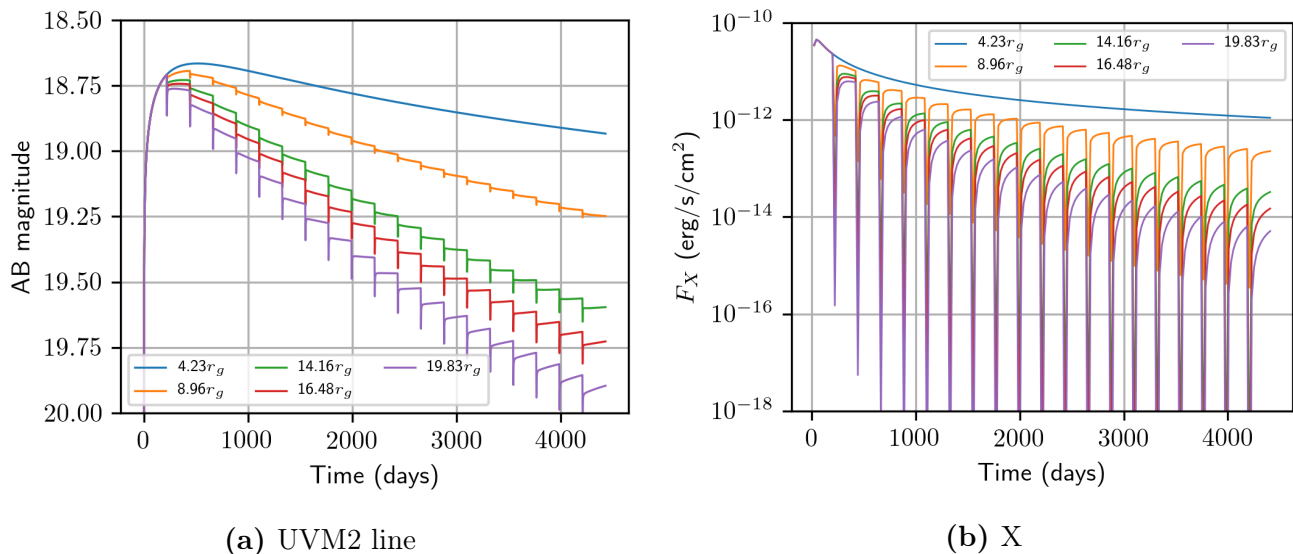


**Figure 10:** Here are presented UV and X-rays emission of depleted discs with different depletion parameters. The list of parameters in table 5 correspond to the labels of the curves. I compare the effect of different depletion radius values. The closer to ISCO the depletion radius is, the less effect the depletion has on the UV and X-rays light curves.

We see that it has a double effect on the light curves presented in figure 10. First, like for truncated discs, the overall luminosity, be it X-rays or UV, is dimmer with greater depletion radius. This is because more mass is being removed at each depletion event. This causes the density, including the

peak density, to be lower less after each depletion event too. The gas heats less and is thus less UV and X-bright.

We also see that the fluctuation amplitude is greater for those large depletion radii. For instance the first depletion event of the run with largest depletion radius lowers the X-rays emission by a factor close to  $10^5$  where the run presented in previous subsection had a factor  $\lesssim 10^4$ . This is because most of the high-energy light is coming from the innermost part of the disc. Removing it will dramatically dim the disc until matter flows back inwards. The more matter is removed, the less dense its 'pile' near ISCO will be. Hence less hot and less bright.

We also note that when the depletion radius is the ISCO radius, the light curves are very similar to the usual untruncated, undepleted disc.

Adjusting the depletion radius together with viscous time, the black hole and disc masses would allow having a model with enough parameters to fit a fluctuating source. The depletion radius determines the amplitude of the fluctuations while the masses determine the overall intensity of the emitted light. This could for example model sources like the one presented on figure 5 [Wevers et al., 2019]. This source features a gap of 100 days in detected X-rays emission. This gap could correspond to one of those depletion events. The X-rays emission is most probably only lesser and not completely dimmed.

### 3 Mass conserving fluctuations of the disc

An actual TDE disc is most probably not as simple as the models presented until now are. A way to model possible fluctuations of the disc matter is to slightly change the position of its matter. Here I present a second fluctuation model, with periodic *fluctuation events* taking place every  $T_f$ . The main difference between this kind of fluctuations and the fluctuations presented in the previous section is that these conserve the disc mass. The periodic depletion, by construction, did not conserve the mass as every  $T_d$ , the inner part of the disc was removed.

Here at each depletion event, I take the mass between two radii  $r_i$  and  $r_o$  and change the density distribution of this mass into a gaussian distribution.

$$\zeta(kT_f, r) \mapsto \mathcal{N} e^{-(r-r_c)^2/\sigma_f^2} \quad (42)$$

for  $r$  between  $r_i$  and  $r_o$ , and  $k \in \mathbb{N}$ .  $r_c$  is the radius around which the fluctuation is centred.  $\sigma_f$  is the standard deviation of the gaussian distribution, this correspond to how flat the distribution is. In the following,  $\sigma_f = 0$  means that I used a Dirac delta function rather than a gaussian of finite width.  $\mathcal{N}$  is a free parameter such that the mass in the fluctuating region is conserved. It is such that

$$\int_{r_i}^{r_o} (U^0(r))^2 \frac{\zeta(kT_f, r)}{W_\phi^r} dr = \mathcal{N} \int_{r_i}^{r_o} \frac{(U^0(r))^2}{W_\phi^r} e^{-(r-r_c)^2/\sigma_f^2} dr \quad (43)$$

The mass integral over the rest of the domain is evolving as usual.

Note that in table 5, we have  $r_i > r_I$  the ISCO radius. This is because, when fluctuations happen near the ISCO, the effect is very strong and does not correspond to small departures from the usual lightcurves. Those results are not uninteresting but are left for future work.

Like in both previous modifications to the model of part I, the UV emission is less affected by the fluctuations in density than the X-rays emission is. We can see it on figure 11. Both lightcurves are very similar to those of ASASSN-14li. The UV emission plateaus rapidly and remains constant until the end of the run. The X-rays emission is also not very different from the usual lightcurves. The final luminosity of both UV and X-rays are lower for more peaked fluctuations. Even though

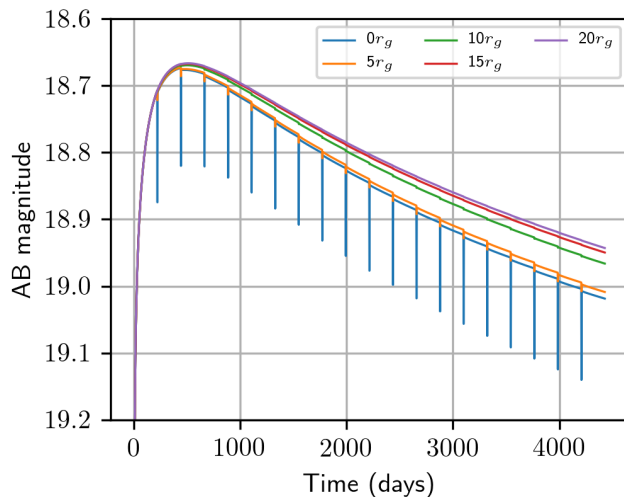
Param.	Value
$a/r_g$	0.5
$M$	$1.85 \times 10^6 M_\odot$
$m$	$1.63 \times 10^{-2} M_\odot$
$\mu$	0
$\eta$	0
$T_f/t_v$	5
$r_0/r_g$	30
$r_i/r_g$	9
$r_o/r_g$	30
$r_c/r_g$	20

(a) Parameters kept constant

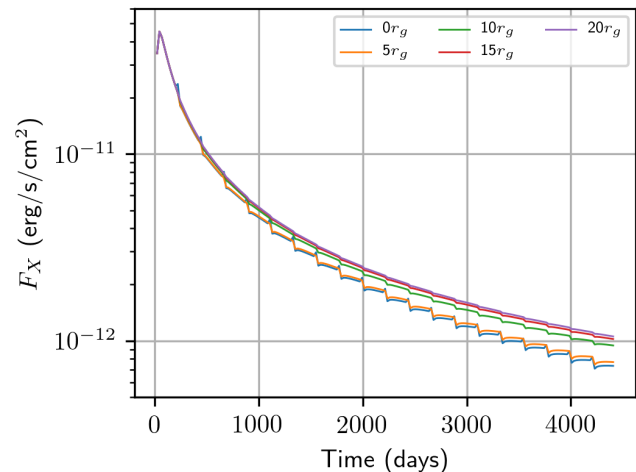
ID	Param.	Value
1	$\sigma_f/r_g$	0
2	$\sigma_f/r_g$	5
3	$\sigma_f/r_g$	10
4	$\sigma_f/r_g$	15
5	$\sigma_f/r_g$	20

(b) Varying parameter

**Table 5:** Parameters used for the comparative runs with fluctuating discs. The constant parameters are the same as in table 3. Here too the values of the parameters are the ones for the fit of ASASSN-14li. Note that run #1 has  $\sigma_f = 0$ , because the mass is put inside a Dirac delta.



(a) UVM2 line



(b) X

**Figure 11:** These plots are lightcurves of UV and X-rays emission of fluctuating discs. The fluctuation parameters are presented in table 5. Here I compare the effect on a periodically fluctuating disc, the effect of the width of the fluctuation. The wider the gaussian distribution of density is, the less effect the fluctuation has on lightcurves. Note that  $0r_g$  width stands for a Dirac delta.

the fluctuation in its self is mass conserving, it will have an influence on the density evolution right after it. A sharper fluctuation will very unevenly distribute matter on the region, taking the mass of the outer fluctuating region at  $r_c$  rather than near  $r_o$  where it should be. This accelerates the mass depletion of the disc by moving the matter closer to the ISCO where mass falls onto the black hole.

The overall effects on the light curves are quite subtle, even for the X-rays emission. This could correspond to the lightcurves of turbulent accretion discs the matter of which periodically take the shape of a gaussian ring for some reason (*e.g.* the gravitational influence of a nearby star, as galaxy centre are the densest parts of a galaxy).

## 4 Conclusion on modifications of the model

Even though the model presented in part I only included simple physics, one can easily modify this model in order to produce more realistic data. I showed how one could explain a late time only X-rays detection, while being consistent with UV emission at early times. I also presented simple model for both mass conserving and not-conserving fluctuation. Those model produce lightcurves with small departures from the usual lightcurves obtained from the model of part I.

## Conclusion

In this report I present how it is possible to produce more realistic theoretical lightcurves for both UV and X-rays emission for transient TDE accretion discs than previous models. I used a fully relativistic disc model [Balbus, 2017]. This model makes use of very well-known physics, namely general relativity, one-dimensional hydrodynamics and Boltzman black-body equation. I solve both analytically and numerically the diffusion-like equation of this model. With the appropriate stress condition at ISCO, this model is known to fit real TDE lightcurves, with powerlaw decay index  $n < 1$  [Balbus and Mummery, 2018]. This model also produces spectral lightcurves which are capable of fitting real transient sources like ASASSN-14li [Mummery and Balbus, 2020]

I then report how new modifications of this model can explain observations that previous models failed to explain. For instance I present how an initial truncation of the disc prevents any X-ray emission while allowing UV emission at early times. This is what is reported by [Jonker et al., 2020], sources that were detected with UV emission only, now appear to feature X-rays emission. I also examine different types of periodic density fluctuations in the disc, both mass conserving and which do not conserve mass. These fluctuations in density achieve to produce fluctuation in the X-rays emission while having a small impact on the UV emission of the TDE accretion discs.

For observers to be able to use those fluctuations model, those shall now be studied in a more quantitative way. In order to know, for a given luminosity fluctuation, how strong a density fluctuation is needed to explain it. The results obtained so far are promising and this work is left for the remainder of this internship and for future works.

## Acknowledgements

I would like to thank Steven BALBUS for guiding me into the exciting world of violent astrophysical events, and showing me how, from an *a priori* horrible mix of hydrodynamics and general relativity one can obtain an actually quite nice and simple model. I am also thankful to him for accepting to go through a internship from home during these dire times and for the time he regularly spent on video calls to follow my progress and give me advices.

I am also very thankful to Andrew MUMMERY for his constant help and physical hindsight on my result. I am also happy that he was able to lead me through the perilous world of coding by precise and helpful advices.

## References

[Auchettl et al., 2017] Auchettl, K., Guillochon, J., and Ramirez-Ruiz, E. (2017). New physical insights about tidal disruption events from a comprehensive observational inventory at x-ray wavelengths. *The Astrophysical Journal*, 838(2):149.

- [Balbus, 2017] Balbus, S. A. (2017). The general relativistic thin disc evolution equation. *Monthly Notices of the Royal Astronomical Society*, 471(4):4832–4838.
- [Balbus and Hawley, 1991] Balbus, S. A. and Hawley, J. F. (1991). A Powerful Local Shear Instability in Weakly Magnetized Disks. I. Linear Analysis. *apj*, 376:214.
- [Balbus and Mummery, 2018] Balbus, S. A. and Mummery, A. (2018). The evolution of Kerr discs and late-time tidal disruption event light curves. *Monthly Notices of the Royal Astronomical Society*, 481(3):3348–3356.
- [Balbus and Papaloizou, 1999] Balbus, S. A. and Papaloizou, J. C. B. (1999). On the dynamical foundations of  $\alpha$  disks. *The Astrophysical Journal*, 521(2):650–658.
- [Cannizzo et al., 1990] Cannizzo, J. K., Lee, H. M., and Goodman, J. (1990). The Disk Accretion of a Tidally Disrupted Star onto a Massive Black Hole. *ApJ*, 351:38.
- [Eardley and Lightman, 1975] Eardley, D. M. and Lightman, A. P. (1975). Magnetic viscosity in relativistic accretion disks. *apj*, 200:187–203.
- [Gammie, 1999] Gammie, C. F. (1999). Efficiency of magnetized thin accretion disks in the kerr metric. *The Astrophysical Journal*, 522(1):L57–L60.
- [Hobson et al., 2006] Hobson, M. P., Efstathiou, G. P., and Lasenby, A. N. (2006). *General Relativity: An Introduction for Physicists*. Cambridge University Press.
- [Holoien et al., 2015] Holoien, T. W.-S., Kochanek, C. S., Prieto, J. L., Stanek, K. Z., Dong, S., Shappee, B. J., Grupe, D., Brown, J. S., Basu, U., Beacom, J. F., Bersier, D., Brimacombe, J., Danilet, A. B., Falco, E., Guo, Z., Jose, J., Herczeg, G. J., Long, F., Pojmanski, G., Simonian, G. V., Szczygie, D. M., Thompson, T. A., Thorstensen, J. R., Wagner, R. M., and Woźniak, P. R. (2015). Six months of multiwavelength follow-up of the tidal disruption candidate ASASSN-14li and implied TDE rates from ASAS-SN. *Monthly Notices of the Royal Astronomical Society*, 455(3):2918–2935.
- [Holoien et al., 2014] Holoien, T. W.-S., Prieto, J. L., Bersier, D., Kochanek, C. S., Stanek, K. Z., Shappee, B. J., Grupe, D., Basu, U., Beacom, J. F., Brimacombe, J., Brown, J. S., Davis, A. B., Jencson, J., Pojmanski, G., and Szczygie, D. M. (2014). ASASSN-14ae: a tidal disruption event at 200 Mpc. *Monthly Notices of the Royal Astronomical Society*, 445(3):3263–3277.
- [Holoien et al., 2019] Holoien, T. W.-S., Vallely, P. J., Auchettl, K., Stanek, K. Z., Kochanek, C. S., French, K. D., Prieto, J. L., Shappee, B. J., Brown, J. S., Fausnaugh, M. M., Dong, S., Thompson, T. A., Bose, S., Neustadt, J. M. M., Cacella, P., Brimacombe, J., Kendurkar, M. R., Beaton, R. L., Boutsia, K., Chomiuk, L., Connor, T., Morrell, N., Newman, A. B., Rudie, G. C., Shishkovsky, L., and Strader, J. (2019). Discovery and early evolution of ASASSN-19bt, the first TDE detected by TESS. *The Astrophysical Journal*, 883(2):111.
- [Jonker et al., 2020] Jonker, P. G., Stone, N. C., Generozov, A., van Velzen, S., and Metzger, B. (2020). Implications from late-time x-ray detections of optically selected tidal disruption events: State changes, unification, and detection rates. *The Astrophysical Journal*, 889(2):166.
- [Krolik, 1999] Krolik, J. H. (1999). Magnetized accretion inside the marginally stable orbit around a black hole. *The Astrophysical Journal*, 515(2):L73–L76.
- [Law et al., 2009] Law, N. M., Kulkarni, S. R., Dekany, R. G., Ofek, E. O., Quimby, R. M., Nugent, P. E., Surace, J., Grillmair, C. C., Bloom, J. S., Kasliwal, M. M., Bildsten, L., Brown, T., Cenko, S. B., Ciardi, D., Croner, E., Djorgovski, S. G., van Eyken, J., Filippenko, A. V., Fox, D. B., Gal-Yam, A., Hale, D., Hamam, N., Helou, G., Henning, J., Howell, D. A., Jacobsen, J., Laher, R., Mattingly, S., McKenna, D., Pickles, A., Poznanski, D., Rahmer, G., Rau, A., Rosing, W., Shara, M., Smith, R., Starr, D., Sullivan, M., Velur, V., Walters, R., and Zolkower, J. (2009). The palomar transient factory: System overview, performance, and first results. *Publications of the Astronomical Society of the Pacific*, 121(886):1395–1408.
- [Lodato and Rossi, 2010] Lodato, G. and Rossi, E. M. (2010). Multiband light curves of tidal disruption events. *Monthly Notices of the Royal Astronomical Society*, 410(1):359–367.
- [Lynden-Bell and Pringle, 1974] Lynden-Bell, D. and Pringle, J. E. (1974). The Evolution of Viscous Discs and the Origin of the Nebular Variables. *Monthly Notices of the Royal Astronomical Society*, 168(3):603–637.
- [Magorrian et al., 1998] Magorrian, J., Tremaine, S., Richstone, D., Bender, R., Bower, G., Dressler, A., Faber, S. M., Gebhardt, K., Green, R., Grillmair, C., Kormendy, J., and Lauer, T. (1998). The demography of massive dark objects in galaxy centers. *The Astronomical Journal*, 115(6):2285–2305.

- [Mummery and Balbus, 2019a] Mummery, A. and Balbus, S. A. (2019a). Evolution of relativistic thin discs with a finite ISCO stress – I. Stalled accretion. *Monthly Notices of the Royal Astronomical Society*, 489(1):132–142.
- [Mummery and Balbus, 2019b] Mummery, A. and Balbus, S. A. (2019b). Evolution of relativistic thin discs with a finite ISCO stress – II. Late time behaviour. *Monthly Notices of the Royal Astronomical Society*, 489(1):143–152.
- [Mummery and Balbus, 2020] Mummery, A. and Balbus, S. A. (2020). The spectral evolution of disc dominated tidal disruption events. *Monthly Notices of the Royal Astronomical Society*, 492(4):5655–5674.
- [Noble et al., 2010] Noble, S. C., Krolik, J. H., and Hawley, J. F. (2010). DEPENDENCE OF INNER ACCRETION DISK STRESS ON PARAMETERS: THE SCHWARZSCHILD CASE. *The Astrophysical Journal*, 711(2):959–973.
- [Novikov and Thorne, 1973] Novikov, I. D. and Thorne, K. S. (1973). Astrophysics of black holes. In *Black Holes (Les Astres Occlus)*, pages 343–450.
- [Paczynski, 2000] Paczyński, B. (2000). The inner boundary condition for a thin disk accreting into a black hole.
- [Page and Thorne, 1974] Page, D. N. and Thorne, K. S. (1974). Disk-Accretion onto a Black Hole. Time-Averaged Structure of Accretion Disk. *apj*, 191:499–506.
- [Phinney, 1989] Phinney, E. S. (1989). Manifestations of a massive black hole in the galactic center. In Morris, M., editor, *The Center of the Galaxy*, pages 543–553, Dordrecht. Springer Netherlands.
- [Press et al., 2007] Press, W. H., Teukolsky, S. A., Vetterling, W. T., and Flannery, B. P. (2007). *Numerical Recipes 3rd Edition: The Art of Scientific Computing*. Cambridge University Press, USA, 3rd edition.
- [Pringle, 1991] Pringle, J. E. (1991). The properties of external accretion discs. *Monthly Notices of the Royal Astronomical Society*, 248(4):754–759.
- [Pringle and Rees, 1972] Pringle, J. E. and Rees, M. J. (1972). Accretion Disc Models for Compact X-Ray Sources. *aap*, 21:1.
- [Rees, 1988] Rees, M. J. (1988). Tidal disruption of stars by black holes of 106–108 solar masses in nearby galaxies. *Nature*, 333(6173):523–528.
- [Shakura, 1972] Shakura, N. I. (1972). Disk Model of Gas Accretion on a Relativistic Star in a Close Binary System. *azh*, 49:921.
- [Shakura and Sunyaev, 1973] Shakura, N. I. and Sunyaev, R. A. (1973). Black Holes in Binary Systems: Observational Appearances. 55:155.
- [von Weizsäcker, 1948] von Weizsäcker, C. F. (1948). Die rotation kosmischer gasmassen. *Zeitschrift für Naturforschung A*, 3(8-11):524 – 539.
- [Wevers et al., 2019] Wevers, T., Pasham, D. R., van Velzen, S., Leloudas, G., Schulze, S., Miller-Jones, J. C. A., Jonker, P. G., Gromadzki, M., Kankare, E., Hodgkin, S. T., Wyrzykowski, L., Kostrzewa-Rutkowska, Z., Moran, S., Berton, M., Maguire, K., Onori, F., Mattila, S., and Nicholl, M. (2019). Evidence for rapid disc formation and reprocessing in the X-ray bright tidal disruption event candidate AT 2018fyk. *Monthly Notices of the Royal Astronomical Society*, 488(4):4816–4830.

## A Numerical methods

### A.1 Radial variable

If we write the evolution equation (10), replacing  $\mathbf{U}$  by its value obtained from the metric, we obtain

$$\frac{\partial \zeta}{\partial t} = \frac{2W_\phi^r}{\sqrt{r_g}(U^0)^2} \frac{\partial}{\partial r} \left[ r^{3/2} \frac{1 - 3\frac{r_g}{r} + 2a\sqrt{\frac{r_g}{r^3}}}{r - 6r_g - 3\frac{a^2}{r} + 8a\sqrt{\frac{r_g}{r}}} \frac{\partial \zeta}{\partial r} \right]. \quad (44)$$

In this equation the radius of the ISCO is singular. The ISCO radius is solution of  $r^2 - 6rr_g - a^2 + 8a\sqrt{rr_g} = 0$  [Hobson et al., 2006]. This renders numerical integration unstable near the ISCO. What

we can do is use an other radial variable, for instance

$$\rho = \left( r - 6r_g - \frac{3a^2}{r} + 8a\frac{r_g}{r} \right)^2 \quad \text{or} \quad (45)$$

$$v = \frac{\rho}{r}. \quad (46)$$

Both variables are bijective functions for  $r > r_{\text{ISCO}}$ , and even if inverting those functions analytically might be hard, doing so numerically is not a problem. One shall nevertheless replace the  $r$  derivatives with the appropriate derivatives in the evolution equation.

$$\frac{\partial}{\partial r} \longrightarrow \frac{\partial \rho}{\partial r} \frac{\partial}{\partial \rho} \quad \text{or} \quad \frac{\partial v}{\partial r} \frac{\partial}{\partial v}$$

The  $\rho$  variable was first proposed in [Balbus and Mummery, 2018], but the  $v$  variable is more convenient for numerical resolution as  $v \sim r$  at infinity, whereas  $\rho \sim r^2$ . Then we see  $r$  as an implicit function of  $\rho$  or  $v$  for the other terms of the evolution equation.

## A.2 Implicit finite difference

In this work I used an implicit finite difference scheme to integrate the diffusion-like equation. Here to examine the numerical method, I use a generic form of the equation

$$\frac{\partial \zeta}{\partial t} = W(r, \zeta) A(r) \left[ B(r) \frac{\partial \zeta}{\partial r} + C(r) \frac{\partial^2 \zeta}{\partial r^2} \right] \quad (47)$$

Note that here  $r$  is a generic name for a radial coordinate, and not the real radial cylindrical coordinate. The functional dependencies of  $A, B, C$  and  $W$  are dropped for clarity.

We use a centred scheme, with  $\mathcal{O}(dr^2)$  error, we use a first order approximation for the time derivative, with error  $\mathcal{O}(dt)$ . I used an implicit scheme, which compared to an explicit scheme, always is numerically stable. However as we will see, one needs to invert a matrix at each time step, making the implicit scheme more computation heavy [Press et al., 2007]. The discretised equation reads

$$\frac{\zeta_r^{t+1} - \zeta_r^t}{dt} = WA \left[ B \frac{\zeta_{r+1}^{t+1} - \zeta_{r-1}^{t+1}}{2dr} + C \frac{\zeta_{r+1}^{t+1} - 2\zeta_r^{t+1} + \zeta_{r-1}^{t+1}}{dr^2} \right]. \quad (48)$$

We can write the associated linear system as

$$\zeta_r^t = \zeta_r^{t+1} \left[ 1 + WAC \frac{dt}{dr^2} \right] + \zeta_{r+1}^{t+1} \left[ -\frac{WAB}{2} \frac{dt}{dr} - WAC \frac{dt}{dr^2} \right] + \zeta_{r-1}^{t+1} \left[ \frac{WAB}{2} \frac{dt}{dr^2} - WAC \frac{dt}{dr^2} \right] \quad (49)$$

$$= \zeta_r^{t+1} \chi_r^t + \zeta_{r+1}^{t+1} \varphi_r^t + \zeta_{r-1}^{t+1} \psi_r^t \quad (50)$$

$$\Leftrightarrow Z^t = M^{(t)} Z^{t+1} \quad (51)$$

$$\Leftrightarrow Z^{t+1} = (M^{(t)})^{-1} Z^t \quad (52)$$

where in equation (51) and (52) we use  $Z^t = {}^T(\zeta_0^t \dots \zeta_r^t \dots \zeta_{N_r-1}^t)$  and we can write the tridiagonal matrix  $M^{(t)}$

$$M^{(t)} = \begin{pmatrix} \chi_0^t & \varphi_0^t & 0 & \dots & 0 \\ \psi_1^t & \chi_1^t & \varphi_1^t & 0 & \dots & 0 \\ 0 & \psi_2^t & \chi_2^t & \ddots & & \vdots \\ & 0 & \ddots & \ddots & \ddots & 0 \\ \vdots & & & \ddots & \ddots & \varphi_{N_r-2}^t \\ 0 & \dots & \dots & 0 & \psi_{N_r-1}^t & \chi_{N_r-1}^t \end{pmatrix}$$

Note that  $\chi, \psi$  and  $\varphi$  depend both on time and space as they are combinations of  $A(r), B(r), C(r)$  and  $W(r, \zeta)$ . This means that if  $W$  does depend on the density, thus on time, the computations gets a lot more heavy as the matrix has to be inverted at each time step. For a time independent  $W$  we have a computation time of order  $\mathcal{O}(N_t N_r^2)$  whereas for a time dependent  $W$  we have  $\mathcal{O}(N_t N_r^3)$ <sup>3</sup>. Note that if  $W$  does not depend on the density,  $M^{(t)} = M^t$  is the usual matrix power.

It is also interesting to see that all boundary conditions for  $\zeta$  are not directly compatible with equivalence of equations (51) and (52). For instance zero boundary conditions render  $M$  singular (with first and last lines set to zero). When we want to impose such boundary conditions (or vanishing gradients), I compute the matrix in its regular way, invert it and only then do I set the values of  $\zeta$  at radii of interest according to the chosen boundary conditions. This has a sensible physical interpretation. For example, in the case of strict boundary condition at the inner edge, this corresponds to matter that fell below the innermost integration radius (the ISCO). This matter is actually lost for the above ISCO system. For strict condition at the outer edge, this is more subtle. Imposing such a boundary condition corresponds to the assumption that the outer edge of the integration domain is far enough that no matter will reach it while the time of the integration. One has to carefully check that this assumption holds at every time step.

### A.3 Simpson integration for non-constant steps

The principle of Simpson algorithm is to integrate a quadratic polynomial interpolation of the function of interest. For a general function  $f$ , we interpolate between three points  $x_1, x_2$  and  $x_3$  where  $f$  takes values  $f_1, f_2$  and  $f_3$  respectively. We define the steps as  $h = x_2 - x_1$  and  $k = x_3 - x_2$ . We require to have two possibly different steps as when integrate physical quantities we shall integrate over the real radial coordinate  $r$  but we used a discretisation such that  $dv = \text{cst}$  or  $d\rho = \text{cst}$ , hence the  $r$  steps are not constant. We aim to solving the following system for  $a, b$ , and  $c$

$$\begin{cases} f_1 = ah^2 - bh + c \\ f_2 = c \\ f_3 = ak^2 + bk + c \end{cases} \quad (53)$$

Note that we approximate  $f(x)$  by  $P(x - x_2)$  a quadratic polynomial function to carry out the integration, such that  $P(x) = ax^2 + bx + c$ .  $P(x_1 - x_2) = f_1$ ,  $P(0) = f_2$  and  $P(x_3 - x_2) = f_3$ . The solution of system (53) reads

$$\begin{cases} a = \frac{kf_1 - (h+k)f_2 + hf_3}{kh(h+k)} \\ b = \frac{-k^2 f_1 + (h^2 - k^2)f_2 + h^2 f_3}{kh(h+k)} \\ c = f_2 \end{cases} \quad (54)$$

Now we switch to a more convenient polynomial function :  $Q(x) = P(x - x_2) = ax^2 + (b - 2ax_2)x + ax_2^2 - bx_2 + c = \alpha x^2 + \beta x + \gamma$ . Hence

$$\int_{x_1}^{x_3} f(x) dx \simeq \int_{x_1}^{x_3} Q(x) dx = \alpha \frac{x_3^3 - x_1^3}{3} + \beta \frac{x_3^2 - x_1^2}{2} + \gamma(x_3 - x_1) \quad (55)$$

The resolution of system (53) has to be carried out every other step as  $h$  and  $k$  are not constant. An example is plotted on figure 12.

---

<sup>3</sup>The usual computation time growth for a  $n \times n$  matrix inversion is  $\mathcal{O}(n^3)$ . I did not use a algorithm specific to tridiagonal matrices.

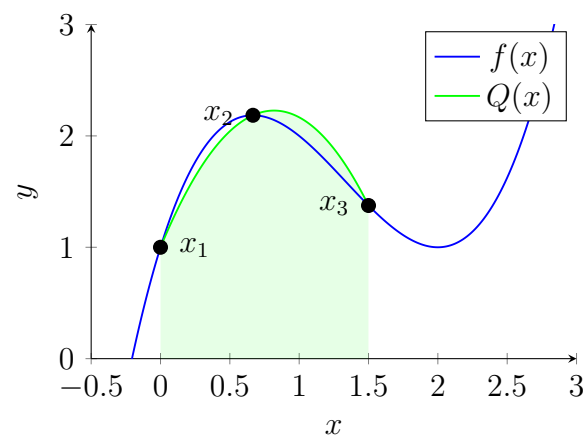


**Figure 12:** This is an example of interpolation of a function  $f$  by a quadratic polynomial function  $Q$ . The coloured area in light green corresponds to the approximated integral of  $f$  between  $x_1$  and  $x_3$ .